

Effects of propagation-induced pulse stretching in airborne laser hydrography

Gary C. Guenther

National Ocean Service, NOAA
Rockville, Maryland 20852

and

Robert W. L. Thomas

EC & G/Washington Analytic Services Center
Riverdale, Maryland 20737

Abstract

Monte Carlo simulation techniques have been applied to underwater light propagation to calculate the magnitudes of propagation-induced depth measurement bias errors as well as spatial beam spreading and signal attenuation for airborne laser hydrography. The bias errors are caused by the spatial and subsequent temporal dispersion of the laser beam by particulate scattering as it twice traverses the water column. Beam spreading results dictate spatial resolution at the bottom and the receiver field-of-view requirement. Sample temporal response functions are presented. The peak power attenuation relationships developed can be used to predict maximum penetration depths. Predicted depth measurement biases are reported as functions of scanner nadir angle, physical and optical depths, scattering phase function, single-scattering albedo, and receiver field of view for several diverse signal processing and pulse location algorithms. Bias variations as a function of unknown (in the field) water optical parameters are seen to be minimized for limited ranges of nadir angles whose values depend on the processing protocol. Bias correctors for use on field data are reported as functions of nadir angle and depth.

Introduction

The basic premise of airborne laser hydrography is that the water depth can be determined by measuring the round-trip transit time for a short duration light pulse. The pulse is envisioned as travelling to the bottom and back to the surface along a fixed path at a known angle from the vertical. This simple model does not take into consideration the spatial and temporal spreading of the beam in the water caused by scattering from entrained organic and inorganic particulate materials.

Analytical computations¹ indicated the existence of a significant depth measurement bias toward greater depths for operations of an airborne laser hydrography system at nadir. The bias arises from a lengthening of the total integrated path length due to the multiple-scattering transport mechanism by which the laser radiation spreads as it traverses the water column. This is the so-called "pulse stretching" effect. For off-nadir beam entry angles, the assumed or "reference" path is the unscattered ray in the medium generated by Snell's Law refraction at a flat surface. There is a propensity for the core of the downwelling energy distribution to be skewed away from this path toward the vertical into the so-called "undercutting" region, due to the fact that the average path length is shorter, and hence the attenuation is less. The energy returning from this region tends to arrive at the airborne receiver earlier than that from the reference path for the same reason. This causes a depth measurement bias toward the shallow side. These two opposing biases superpose to yield depth estimates which, although they depend on water optical properties, are generally biased deep for small beam entry nadir angles and shallow for large nadir angles. The net biases can greatly exceed international hydrographic accuracy standards.

The key to quantification of the effects of scattering is the generation of a set of response functions for the propagation geometry which characterize the temporal history of radiation reaching the receiver for an impulse input. Although various analytic approximations can be achieved via simplifying assumptions, the actual formal problem is effectively intractable due to the complexity of the multiple scattering. Monte Carlo simulation is a practical method of generating the needed impulse response functions (IRFs). A powerful new Monte Carlo simulation technique has been developed and exercised to model the effect of underwater radiative transfer processes on airborne lidar signals for impulse laser inputs to homogeneous and inhomogeneous water columns. The water parameters and systems constraints of the computations are appropriate to airborne laser hydrography systems presently under consideration for use in coastal waters. Simulation results include full sets of spatial and temporal distributions. Horizontal resolution at the bottom and receiver field-of-view requirements are derived from the spatial results.

The impulse responses from the simulation have been convolved with a realistic source pulse to yield expected bottom return signal characteristics, the so-called environmental response functions (ERFs) at a distant, off-nadir airborne receiver. Appropriate volume backscatter decay has been added to the leading edge of each ERF. Depth measurement biases have been estimated by applying realistic signal processing and pulse location algorithms to the augmented ERFs. Resulting outputs are pulse shapes, peak power, and, most importantly, depth measurement bias predictions. Bias sensitivities to input parameters are examined in detail. It is important that the propagation-induced depth measurement biases be accurately calculated, because if the predicted biases do exceed an acceptable magnitude, they can, at least conceptually, be applied to field data as bias correctors in post-flight data processing to maintain system performance within the error budget.

In the Monte Carlo approach, the transport of photons to the bottom is modeled as a series of individual, random scattering and absorption events in the water column. Spatial and temporal distributions of photons arriving at the bottom are accumulated over a large number of representative paths. These distributions are then manipulated analytically to produce the estimated response at a distant airborne receiver.

Traditionally, the mean free path for radiation transport through water is described through a parameter called the "narrow-beam attenuation coefficient", $\alpha(\lambda)$, which is comprised of two components: scattering and absorption. If "s" is the scattering coefficient and "a" is the absorption coefficient, then $\alpha(\lambda) = a(\lambda) + s(\lambda)$. The values of these water optical properties depend strongly on wavelength, λ . For coastal waters, the minimum attenuation occurs in the green. Airborne bathymetric lidar systems operate in the green in order to maximize depth penetration potential. In this report, the wavelength dependence of the water parameters will not be explicitly shown, and all reported numeric values will be appropriate for green wavelengths. If a monochromatic beam of radiance, N_0 , is incident on a column of water, then the amount that remains neither scattered nor absorbed after travelling a distance, d , is $N_0 \exp(-\alpha d)$. Since the mean of the exponential occurs at $\alpha d = 1$ the mean free path, q , is equal to α^{-1} . The vertical "optical depth" of the medium, defined as the number of mean free path lengths required to vertically traverse the medium to the bottom for a depth, D , is D/q which is thus equal to αD . In the simulation, the distance between scattering events is assumed to be exponentially distributed with a mean free path, q . Individual path lengths, L , are generated from the expression $L = -q \ln \rho$, where ρ is a rectangularly distributed random number in the interval $(0,1)$. The "albedo for single scattering", ω_0 , is the average fraction of the incident energy at each scattering event that is not absorbed: i.e., $\omega_0 = (\alpha - a)/\alpha = s/\alpha$. For typical coastal waters, ω_0 ranges from about 0.55 to 0.93 at green wavelengths. In the simulations, photons are not actually eliminated by absorption as they might be in the real world. Following the method of Plass and Kattawar², their behavior is represented by retaining photon weights (initially unity) which are multiplied by a vector of ω_0 values at each scattering event. In this way, the photons are not removed from the simulation, and results can be conveniently accumulated for many values of ω_0 at the same time.

Photons change direction at all scattering events. The scattering angle ψ from the incident direction is generated according to the "phase function", $P(\psi)$, which defines the probability that the photon will scatter into a unit solid angle at ψ . Since the solid angle between ψ and $\psi + d\psi$ is $2\pi \sin\psi d\psi$, the probability of occurrence of ψ in that range is $p(\psi)d\psi = 2\pi \sin\psi P(\psi) d\psi$. Note that the phase function is simply the "volume scattering function" normalized to exclude specific water clarity conditions by dividing by the scattering coefficient, "s". The random value of each simulated scattering angle, ψ_k , is generated by tabulating values of the normalized integral of $p(\psi)d\psi$ from 0 to ψ_k as a function of ψ_k and sampling the results with values of ρ , for ρ as above. Typical phase functions³ for water at green wavelengths exhibit very strong forward scattering. For the simulations, two bounding phase functions for coastal waters designated "NAVY" or "clean" (Petzold HAOCE-5) and "NOS" or "dirty" (Petzold NUC-2200) were utilized. These phase functions increase by a factor of more than 1,000 as the scattering angle diminishes from 10° to 0.1° . Roughly a quarter of the scattering occurs at angles of less than 1° , and three-fourths is under 10° . Scattering results both from opaque inorganic particles and translucent organics. Size distributions vary widely with location. The large forward scattering observed indicates⁴ that the dominant scatterers are inorganics of over micron size as well as organics of various sizes.

The "inherent" parameters α , ω_0 , and $P(\psi)$, along with D , are the independent descriptors of the transport medium characteristics required as inputs by the simulation and are thus also the optical properties upon which the biases are ultimately parameterized. The relationships between these parameters and the parameters governing the "apparent" properties of the medium have been discussed by Gordon, Brown, and Jacobs⁵. The most important apparent optical parameter is $K(\lambda)$, the so-called "diffuse attenuation coefficient," which is defined as the fractional rate of decay of the downwelling flux with depth. For small depths, K depends on both the depth itself and the angle of incidence of the radiation at the surface; but for larger depths these dependences become very small, and K approaches an asymptotic value. The ratio, K/α , for typical natural waters, is a monotonically decreasing function of ω_0 , which has a value of unity when ω_0 is zero and which decreases to zero slightly above a unit slope line as ω_0 tends to unity^{6,7}. There are small dependences on the phase function and optical depth, but these are unimportant for applications in coastal waters. The energy loss of the downwelling beam as a function of depth, and hence the maximum useable "penetration" depth for a laser system, is most easily described in terms of K . In a similar fashion, K dictates the intensity and rate of decay of the volume backscatter signal preceding the bottom return. The biases, however, are not functionally dependent on K or KD , but rather on αD or $\omega_0 \alpha D$ ($=sD$). Combinations of α and ω_0 which produce the same value of K do not yield the same biases.

In order to calculate the IRF at a distant, off-nadir receiver, one must know the time history of each returning photon and its location in the upwelling surface distribution. By invoking reciprocity⁸, the upwelling paths are generated by applying Lambertian weighting to the downwelling paths. Reciprocity is a statement of symmetry or reversibility which, when applied to airborne lidar, implies that the ensemble of viable scattering paths in the water is identical for downwelling and upwelling radiation, because the exiting photons must leave the medium in the opposite direction from which they entered in order to reach the distant receiver colocated with the laser source. One can form each possible round-trip path by pairing each downwelling path with each upwelling path. An important gain in the information content of the results arises from the realization that, for given values of αD and ω_0 , all IRF results scale linearly with the depth. Photon paths for cases with the same αD but different D are geometrically "similar" so that the fractional time delays are identical, and one set of normalized response functions can be used to generate absolute results for all depths.

Propagation delay times of paired paths are combined with their appropriate geometric air-path delays from the surface to the receiver. For selected fields of view, histograms of these total transit delay times are formed to produce the receiver IRFs. The variation in the air-path length to the distant receiver across the upwelling surface distribution is an important effect which significantly alters the shape of the IRF, except perhaps at nadir where the air-path variation is not as great. For off-nadir angles, the shortest total round-trip path is not the one including a vertical path to the bottom, but rather, due to the shorter air path, one in which the photons arrive at the bottom closer to the aircraft. Thus, highly scattered energy

actually defines the leading edge. Since the set of all possible path pairs is not statistically independent, a smaller subset of these pairs can be used, to save computer time, with very little loss in information. Several variations of photon number and pairing combinations were examined in order to find the most cost-effective approach. Reported results are based on 1000 downwelling photon paths were paired with a block of 25 randomly selected upwelling paths for a total of 25,000 round-trip paths. The resulting IRFs are somewhat noisy for cases of high attenuation, i.e., concurrent low ω_0 and high αD . A larger number of photons and/or pairings would be beneficial, but a much larger set would be required to significantly improve performance.

The simulations were primarily performed for homogeneous water in which the density and nature of the scattering particles are independent of depth, because tests with extreme surface and bottom inhomogeneities⁹ produced differences of less than ± 10 cm in the predicted depth measurement biases. For each of the two phase functions, six simulation runs with nadir angles in air of 0, 10, 15, 20, 25, and 30 degrees were performed. To ensure comprehensive results sets, simulations over full ranges of αD (2-16) and ω_0 (0.4-0.9) were run for each case. Five values of optical depth and four values of single-scattering albedo were employed in each simulation run. Spatial and temporal bottom distributions were printed for each case. A data base containing 240 normalized impulse response functions, each resolved into 50 time bins, has thus been created. The durations of the IRF leading and trailing edges are seen to increase substantially as nadir angle, optical depth, and single-scattering albedo increase.

For finite source pulses, realistic lidar receiver inputs or environmental response functions (ERFs) are calculated by convolving a selected source function with the appropriate impulse response functions. ERFs have been computed by digitally convolving the IRFs, scaled to depths of 5 m, 10 m, 20 m, and 40 m, with a 7-ns (FWHM) triangular source pulse which is representative of laser pulses from a state-of-the-art, high repetition rate, frequency-doubled Nd:YAG laser. Much of the simulation noise evident in the IRFs is smoothed out by the convolution. Depth measurement biases for twelve different combinations of signal processing and pulse location algorithms have been calculated from these ERFs. The ERFs and their associated peak powers and biases are archived on magnetic media for future use. In the bounding cases, the ERFs for very narrow IRFs are similar to the source pulse; while for broad IRFs, the ERFs are similar to the IRFs. Most cases of practical application lie between these limits, and the ERF shapes are a unique combination of both. For a source function significantly different from a 7-ns triangle, the ERFs and resulting biases would need to be recomputed by convolving the new source function with the depth-scaled, archived IRFs.

Spatial resolution and receiver field of view

Scattering in the water column causes the incident beam to spread out spatially into an expanding cone. The extent of the spreading depends in a complex manner on the geometry, the optical depth, the phase function, and the single-scattering albedo of the water. For off-nadir angles, the energy density distribution is significantly skewed toward the vertical due to reduced attenuation. The skewness is more pronounced for higher optical depths, higher off-nadir angles, and more highly scattering phase functions such as "NOS". This early-arriving energy has a large effect on the shape of the IRF.

Energy distributions for a planar detector (consistent with airborne laser hydrography geometry) have been estimated as an output of the Monte Carlo propagation simulation. Plots of 50% energy and 90% energy bottom distribution diameters, d_b , normalized to a vertical water depth, D , are shown in Fig. 1 (left axis) for nadir entry and several values of ω_0 . The curves, which are averaged between NAVY and NOS phase functions, are labeled by the n^{th} percentile energy fraction contained within. Curves for RMS diameters fall between the two values illustrated. A notable and important characteristic of these curves is that they tend to saturate at large optical depths. This is fundamentally different from Duntley's results¹⁰ to a spherical cap which continue to rise with increasing optical depth. This behavioral difference is attributed to the disparate geometries. In the Duntley experiment, the off-axis radiation traversed the same path length as the on-axis radiation. For a planar target, the added attenuation length for non-axial paths causes a significant reduction in the signal magnitude received at larger angles. This results in a reduction of the effective "spot" diameter — particularly for large optical depths. For the large optical depths, the simulation results indicate that the diameter of the 50% energy fraction at the bottom is roughly half the water depth, and the diameter of the 90% energy fraction is somewhat greater than the water depth. Mean and RMS diameters fall between these bounds.

Although one thinks of a laser beam as being a highly collimated probe, such is not the case in water. The beam is scattered by entrained particulates into an expanding cone whose size increases as the optical depth of the medium increases. Based on the above downwelling results, the effective angular beam width at the bottom for a 50% energy fraction is about $2 \tan^{-1}(0.25) = 28^\circ$. This means that an airborne lidar will not provide detailed profilometry with a horizontal resolution of several meters at typical operating depths in the 20 m - 40 m range. The soundings, rather, are center-weighted averages over an area with a diameter of roughly half the water depth. This fact is somewhat misleading, however, in that small but not insubstantial shoal objects such as coral heads or large rocks will nevertheless reduce the measured depth because leading edge pulse location algorithms are sensitive to the early-arriving energy. If somewhat higher resolution were required for some special task, a narrower effective beam width could be obtained by limiting the receiver FOV. The tradeoff is a concomitant loss of peak return power and, hence, penetration capability. In optically shallow waters, this loss might be an acceptable compromise.

Because of reciprocity, the diameter of the surface distribution of reflected bottom energy can be derived from the convolution of the bottom energy density distribution with a slightly modified version of itself. The resulting surface diameter of upwelling bottom return energy will be somewhere between one and two times the equivalent bottom diameter, depending on the exact shape of the distribution. For a Gaussian distribution, the factor is $\sqrt{2}$. Surface diameters for this approximation are indicated on the right-hand axis of Fig. 1. For an estimated surface diameter, d_s , of the selected bottom-reflected energy fraction for nadir entry, the 50% energy criterion is $d_s(50) \approx 0.7D$, and the 90% criterion is over twice that. The field-of-view (FOV) requirement can be seen to depend strongly on which measure of "spot size" is used.

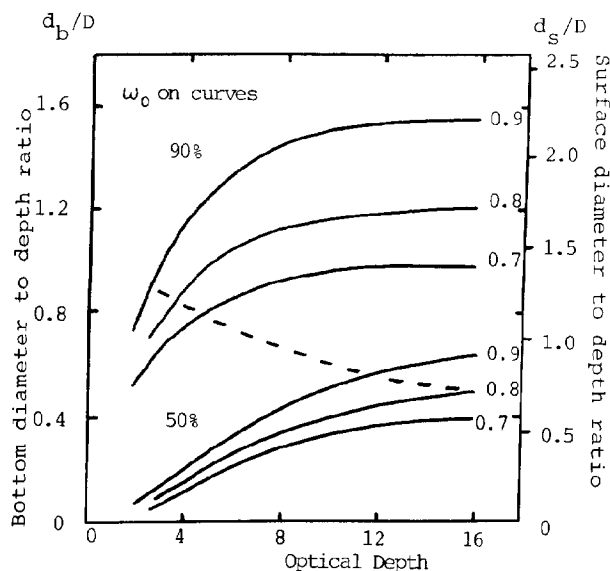


Figure 1. Bottom and surface energy distribution diameters for 50th and 90th percentiles. Dotted line represents estimate for maintaining received peak power.

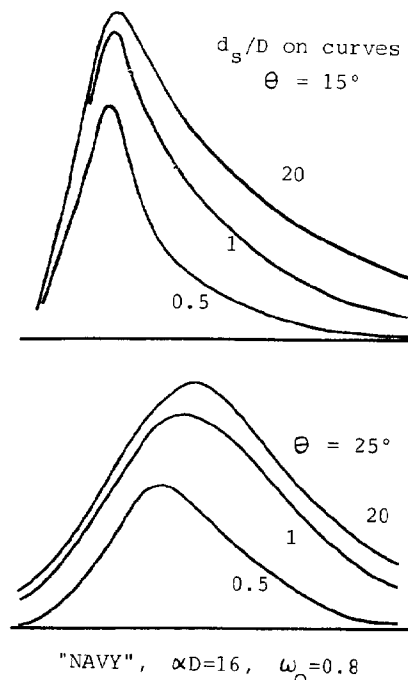


Figure 2. Field-of view-effect on impulse response functions.

The primary effect of the FOV is the determination of the bottom return signal-to-noise ratio (SNR) and, hence, the maximum useable depth or "penetration" capability. If the FOV is too small, the peak bottom return power and associated maximum penetration depth will be reduced. For nighttime operation, a larger than necessary FOV is benign, but in daylight, an excessive FOV will increase the solar noise level and, again, reduce penetration. The FOV "requirement" is thus the FOV which maximizes the SNR or, more simply, that which is just large enough not to significantly reduce the peak bottom return power. For small physical and optical depths, say two to four, the IRF is short, the ERF approximates the source pulse, and any loss of energy results directly in a loss of peak power. For this case, therefore, the d_b/D required would derive roughly from the d_{90} curves. For large physical and optical depths, the ERF takes the character of the IRF and is significantly wider than the source pulse. Moderately restricting the FOV will reduce the pulse energy, but not the peak power, by truncating the tail of the IRF, as seen in Fig. 2. This is a beneficial feature because, in deep water where the FOV requirement is the greatest, the pulse stretching is also greatest. A modest fraction of the pulse energy from the trailing edge can be discarded without a significant drop in the peak pulse power — thus reducing the necessary energy fraction and the actual FOV requirement. By examining the effect of reduced FOV on such IRF shapes, it has been noted that the peak height is not significantly reduced until d_b/D becomes less than about 0.7, which, from Fig. 1, corresponds roughly to a 50% energy fraction. The dotted line drawn across Fig. 1 is an estimate of the overall d_b/D requirement according to these arguments. The function rises only slightly toward small optical depths because, even though the required energy fraction is larger, the relative expansion of the beam due to scattering is less.

For a practical system, the receiver FOV can be safely set to the high αD value where d_b/D is smallest, since at smaller optical depths a slight loss of power will not significantly affect performance. The best estimate for a practical FOV requirement is thus a surface spot diameter for the receiver of about 0.7D which corresponds roughly to a 50% energy criterion at large optical depths, as previously noted. For an aircraft altitude, H, the necessary full angle FOV would be $d_b/H \approx 0.7D/H$. The FOV desired for a typical aircraft altitude of 300 m and a depth of 35 m would thus be about 80 mr. A FOV of this size is fairly large for a compact optical system, but nevertheless achievable. This result is relatively independent of nadir angle. For off-nadir angles θ in air and ϕ in water, the irradiated bottom dimension is larger roughly by $\sec \phi$ due to the additional slant distance to the bottom, but the FOV needed to encompass the resulting surface spot is smaller by $\cos \theta$. For the relatively small angles of interest, these functions effectively cancel.

The effect of FOV on propagation-induced biases is small. The reason for this is the fact that significant biases would exist even for zero FOV (ignoring, for a moment, the corresponding lack of signal strength), because the leading edges of the IRFs are not greatly affected by FOV. The concept that the IRF has a certain minimum width for zero FOV stems from the fact that photons emerging from the medium at the point of entry may have undergone substantial multiple scattering and consequential pulse stretching on their round trip to the bottom and back. Reciprocity in this case requires that the photons must effectively retrace their downward paths to exit the medium at their entry points in the exact opposite direction. In this special case, the convolution of the downwelling distribution with a cosine-modified version of itself degenerates into a simple product with the times doubled for the round trip. This concept has been used to estimate the zero-FOV IRFs from the downwelling temporal distributions. The leading edges of the IRFs are not greatly altered from the large FOV case, and the depth measurement biases are not greatly reduced.

Energy and peak power relationships

The economic viability of an airborne laser hydrography system depends on the existence of large areas of relatively shallow water from which satisfactory bottom returns can be detected. The level at which the signal becomes unacceptably noise contaminated determines the maximum range. The shape, duration, and magnitude of laser hydrography bottom returns depend in a complex way on the source pulse, the beam nadir angle, the depth of the water, the optical properties of the water, and the bottom topography. In order to predict penetration limitations for an operational system, temporal response functions at the airborne receiver for a flat bottom have been calculated from the Monte Carlo simulation results.

The bottom reflected pulse energy, E_R , returned to a distant, airborne receiver was calculated by temporally integrating the round-trip impulse response functions derived from the simulation for an assumed Lambertian bottom reflection. For a large receiver FOV, this received pulse energy can be represented as $E_R \propto \exp(-2KD)$. Considering reciprocity, this is indicative of the fact that the Lambertian weighting function for the bottom reflected upwelling distribution is similar to the downwelling arrival angular distribution. Since pulse detections are based on the instantaneous pulse power, not the integrated pulse energy, the received energy equation must be converted to one which describes the peak pulse power. It is clear that peak power and pulse energy are proportional, i.e., obey the same functionalities, as long as the pulse shape remains unchanged. Pulse stretching removes that proportionality. Although the pulse may contain the same total energy, the fact that it is distributed over a longer time interval causes its peak power to be reduced. Furthermore, for a fixed αD , the absolute amount of stretching of the impulse response function is, from simple geometry, linearly proportional to the physical depth, D . For this reason, underwater propagation causes not only a loss of energy as a function of optical depth, but the associated pulse stretching causes a further loss of peak power with respect to the pulse energy, which varies both as a function of the physical depth and the inherent optical parameters.

Specific peak power results have been generated for ERFs obtained by convolving the Monte Carlo-derived IRFs with a 7-ns (FWHM) triangular source pulse. For $\alpha D < 16$ and to depths of at least 40 m, the peak power results can be described simply by exponentials with an effective increase in the system attenuation coefficient of the form $P_R \propto \exp(-2nKD)$, where, in general, $n = n(s, \omega_0, \theta)$. The values of $n(s, \omega_0, \theta)$ are derived from semi-log plots of peak power versus optical depth for various fixed values of θ , ω_0 , and α . The slopes of these lines are quite constant except at very low αD , and the nadir angle effect is quite small. Because the preferred paths in the core of the downwelling distribution curve rapidly toward the vertical at moderate optical depths, the slopes are modeled as $-2nK/\alpha$ with no explicit secant of the water nadir angle. By measuring the slope and knowing K/α from ω_0 , one can determine the values of n . In this way, any residual, unmodeled nadir angle effects are automatically included in the calculated value of n .

The dependence on the scattering phase function is small except at $\omega_0 = 0.9$. The nadir angle effect is quite small, and the majority of bottom return peak power loss with increasing off-nadir angle thus arises simply from the $\cos^2 \theta$ term in the solid angle ratio. Various levels of approximation may be used for describing n depending on the estimation accuracy desired. A decent first-order approximation for natural waters is $n \approx 1.25$ for all cases. A slightly better fit, good to ± 0.1 , is provided by the expression $n \approx 1 + 0.27 \alpha^{0.24}$, valid for all θ and ω_0 but limited to $\alpha \leq 2 \text{ m}^{-1}$. A more detailed fit can be obtained, if desired, in the forms $n = A \alpha^{-B}$ or $n = A s^{-B}$. The latter is more rigorous phenomenologically and was adopted. The most straightforward fits are obtained with the A's and B's expressed not directly in terms of ω_0 , but rather in s/a which is equal to $\omega_0/(\omega_0 - 1)$. The selected model is thus

$$n(s, \omega_0, \theta) = A(s/a, \theta) s^{-B(s/a, \theta)}. \quad (1)$$

The coefficients A and B can be expressed in the forms $A = c_1 + c_2(s/a)$ and $B = c_3(s/a)^{c_4}$. The fits for various ranges of beam entry nadir angle are found in Table 1.

θ	c_1	c_2	c_3	c_4
$0^\circ - 15^\circ$	1.02	0.032	0.032	0.79
$15^\circ - 25^\circ$	1.03	0.035	0.042	0.69
25°	1.05	0.036	0.050	0.60
35°	1.11	0.024	0.072	0.54

Table 1. Regression coefficients for exponential power decay factor.

The curves of P_R versus αD for fixed α are slightly flatter at small αD 's where they approximate the energy case. The extrapolated slopes from higher αD thus intersect the P_R axis ($\alpha D = 0$) slightly above the actual value of P_T . To correct for this effect, the ratios of the extrapolated slope intercepts have been calculated and denoted as "m" such that $P_R \propto m P_T \exp(-2nKD)$. To a first order, one might simply select $m \approx 1.25$. In reality, the magnitude of this effect is small and compensates for such things as ignoring air path losses and a little optical system detuning; and it may practically be ignored.

For a practical case with a 7-ns source pulse, the peak power received from the bottom return, obtained by converting the received energy equation, may thus be described as

$$P_R = P_T \eta R F \left[\frac{A_R \cos^2 \theta}{\pi (n_w H + D)^2} \right] e^{-2 n(s, \omega_0, \theta) K D}, \quad (2)$$

where: P_T is the transmitted pulse peak power, η is the total optical system loss factor, R is the bottom reflectivity, F is a loss factor to account for insufficient receiver FOV, A_R is the area of the receiver aperture, H is the aircraft altitude, n_w is

the index of refraction of the water, and the n 's are as previously reported. The bracketed solid angle ratio is a simplified form approximated from the full expression in Levis et al.¹¹ An insufficient FOV which spatially excludes a portion of the returning signal reduces the F factor below unity in a highly complex way which depends on the FOV, water parameters, depth, altitude, and the duration of the incident source pulse. No detailed relationships have been derived for F other than to note, as in the previous section, the FOV required to maintain a value near unity. This effect could alternately be viewed as an increase in the effective system attenuation coefficient.¹²

This signal rides atop the volume backscatter signal which decays at the same rate with increasing depth. From this form, it can be seen that a so-called "extinction coefficient", ξ_m , expected to be fairly constant for all water conditions (for a given system with specified altitude, nadir angle, etc.) can be defined in the form $\xi_m = nKD$. It is important to reiterate here (because of confusion and expediencies in the past) that neither the bottom return energy nor the peak power depend unambiguously on the optical depth, αD . The optical depth alone cannot be used to predict maximum penetration depths because these are seen to depend explicitly on KD , and the relationship between K and α is a very strong function of ω_0 . Pulse stretching adds an additional loss factor which has been characterized as an increased exponential loss factor.

Bias prediction

Bias computation

For a given set of depth-specific, simulated bottom returns (ERFs) parameterized on beam nadir angle and water optical properties, the first step in calculating depth measurement bias predictions is the modeling of the various signal processing and pulse location estimation procedures. After the appropriate transfer functions have operated on the input signals, the apparent depth is calculated from the time interval between the detection locations of the surface return and bottom return pulses. For the reported biases, the source pulse was used directly as the surface return pulse (a mirror-like reflection from a flat surface), and a common pulse location algorithm was applied to each. It is conceivable that separate optimization of the surface and bottom return detection algorithms might be desirable. If so, locating the two pulses at different thresholds, for example, would cause an additional bias which depends only on the shape of the interface return and which could be removed with a pre-calculated corrector. The simulation error in all reported biases is estimated to be ± 5 cm.

Biases were calculated for all combinations of physical depth, receiver parameters, and relevant water optical properties (phase function, optical depth, and single-scattering albedo) for two diverse types of pulse location algorithms: a straightforward fractional amplitude threshold (proportional to the peak height) applied to the linear input (designated "LFT") and the complex HALS protocol¹³ (planned for the U. S. Navy's Hydrographic Airborne Laser Sounded) which involves logarithmic amplification for amplitude compression, a time-delayed difference operation to remove the volume backscatter signal, and pulse location by a specialized constant fraction discriminator (CFD) algorithm as implemented on an available hardware chip. Each basic algorithm is represented by multiple sets of biases corresponding to selected values of imbedded parameters. Linear fractional threshold detections are obtained directly from the ERFs. Because the HALS processing involves two time-delayed differences, however, the resulting pulse detection time depends not only on the shape of the ERF, but also on the log slope of the volume backscatter signal which precedes it. The effect can be quite significant in "dirty" waters where the backscatter slope is steep. In order to provide accurate bias predictors for the case of HALS processing, the specific volume backscatter signal associated with each ERF has been appended to the start of that ERF. For a given ERF, the parameters αD , D , and ω_0 are specified. The value of α is thus known, and given ω_0 , the K/α ratio is known. K is thus uniquely defined for each ERF. Like the bottom return peak power, the volume backscatter decay is exponential in time with a log slope of $-nK$, where c is the speed of light in water and $n \approx 1.25$ is the same "constant" factor (derived from analysis of the ERF normalizations) as in the received power equation. For HALS processing, the volume backscatter signal for each ERF is constructed in log space by extrapolating a line of appropriate slope backward from the first point of the logged ERF.

Bias sensitivities

The bias differences with phase function for nadir angles of at least 10° are typically under 10 cm, which is small enough that an average value between the two can be used for bias prediction. As pointed out by H. S. Lee¹⁴, the most compact form for biases is in terms of the scattering optical depth, $sD = \omega_0 \alpha D$. In this representation, ω_0 is effectively removed as a separate free parameter. This follows from the work of Wilson¹⁵ who demonstrated that functionality for the radiance and irradiance distributions. The effects of the air nadir angle at a 20-m depth for the NAVY phase function is seen in Fig. 3 for LFT(50%) pulse location and a FOV corresponding to $d_g/D=1$. Note the orderly progression toward more negative (shallow) biases as the nadir angle increases. This is due to the proportionately larger effect of "undercutting" at larger incident angles. The effect of physical depth for the same parameters at a constant nadir angle of 20° is illustrated in Fig. 4. Note the tendency toward larger biases (both positive and negative) at larger physical depths due to the fact that the depth acts as a scaling factor for the normalized time delays. HALS (log/difference/CFD) processing has a disadvantage in that there is an additional degree of freedom in the bias dependency — the so-called P_m/B ratio which is a measure (in linear space) of the peak signal-to-background ratio. If P_m/B is not specified in the bias correction procedure, an additional ± 10 cm uncertainty will result. It will be seen shortly that this added error component is unacceptably large if the total bias uncertainty is to be limited to ± 15 cm, and for this type of processing, P_m/B will need to be estimated for each return.

There can be tremendous variation in both the bias trends and magnitudes for different processing and pulse location protocols. The HALS biases for a 6-ns difference delay are consistently more negative due mostly to later detection on the surface return but also partly to earlier detection on the leading edge of propagation-stretched bottom returns. The magnitude of the effect of the difference delay is significantly greater than the effect of the CFD delay. The HALS biases can be moved significantly in the positive direction by increasing the duration of the delay in the difference operation. This causes the nadir angle at which the multiple-scattering and undercutting biases nearly compensate to be increased. The difference delay can thus be used to tune the biases for best performance at the operational nadir angle of interest.

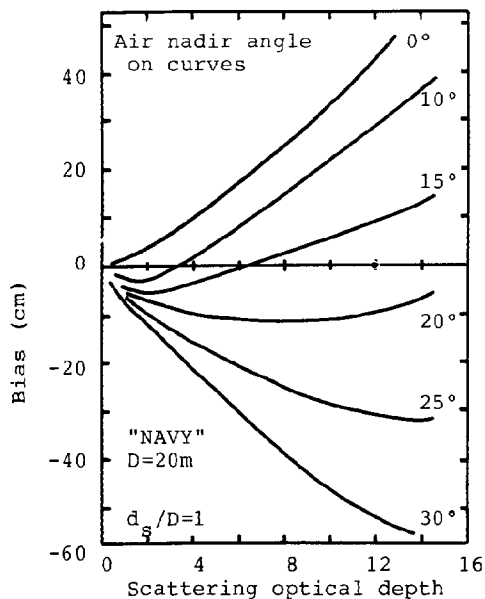


Figure 3. Nadir angle dependence of LFT (50%) biases.

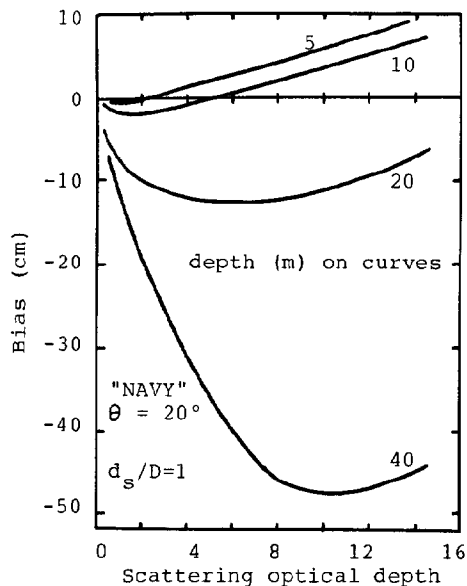


Figure 4. Depth dependence of LFT (50%) biases.

Bias variation

For bias correction purposes, predicted biases can be utilized only to the extent that the driving independent parameters are known. Water optical parameters which are unknown and difficult to estimate in real time from lidar returns are phase function and scattering optical depth. For various combinations of known parameters, the bounding bias predictions, based on total uncertainty in phase function and scattering optical depth, have been extracted from the data base. For this procedure, q_0 values of 0.6 and 0.8 were associated with the NAVY phase function, and 0.8 and 0.9 with the NOS. The optical depth was considered unknown over the range from 2 to 16. For fixed values of nadir angle and depth, the mean values of the bounding bias pairs and the variations from these means to the bounding values have been calculated.

The means of the bounding bias pairs or "mean extrema" biases are the optimum bias predictors from the point of view that they minimize the worst-case bias prediction errors over all unknown water clarity conditions. They are neither the average nor the most probable biases. The variations from the extrema means to the extrema, the so-called "half-ranges," are those worst-case errors. In other words, if the reported mean of the bounding biases for a given nadir angle and depth is used as a "passive" bias corrector, the error in the resulting depth estimate due to the effect of unknown water clarity parameters should never be larger than the reported variation or half-range. If these bias variations can be constrained to acceptable bounds by the selection of appropriate ranges of operating variables, then precalculated mean biases can be applied to measured depths as correctors, and water clarity parameters need not be estimated from field data.

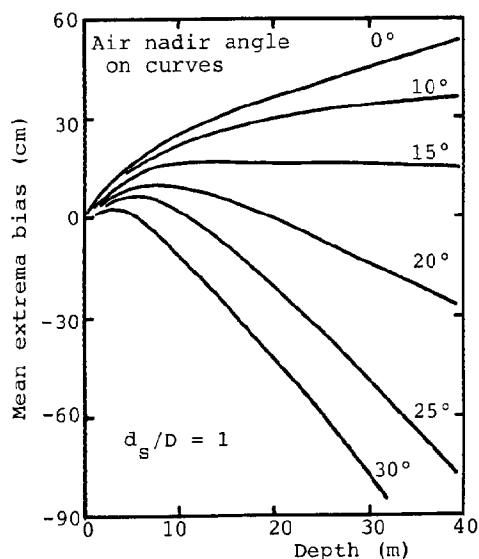


Figure 5. Mean extrema biases for LFT (50%).

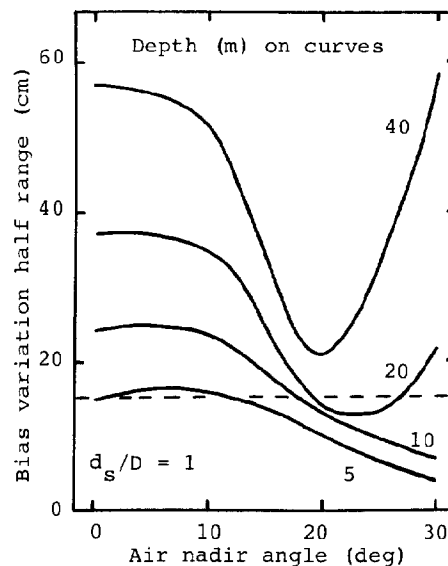


Figure 6. Bias variation half ranges for LFT (50%).

The magnitudes and functionalities of the bias extrema means and half-ranges about the means for the LFT(50%) case is presented in Figs. 5 and 6 as a function of nadir angle for depths from 5 to 40 m and for a FOV corresponding to $d_s/D=1$. The main feature of this data is the existence of minima in the bias variation curves. These minima occur as the bias trends switch from being lengthened by multiple scattering to being shortened by undercutting. The resulting mean biases for these bias variation minima are thus generally fairly small. At a 20-m depth, the minimum for this case is at a nadir angle of 23° , and the angle decreases slightly with increasing depth. The critical issue is the magnitude of the bias variation with unknown water parameters. In a total error budget of ± 30 cm, only about 15 cm can be allotted to this error source as noted on Fig. 6 by a dashed line. It can be seen that for this case the bias variations at a 20-m depth are less than 15 cm for nadir angles between 20° and 26° . For 5-m and 10-m depths, bias variations are under 15 cm beyond angles of 13° and 19° , respectively. At 40 m, the minimum variation is 21 cm, and, by interpolation, the 30-m variation is about 17 cm. The half-range curves for a 20% LFT are similar to their 50% LFT counterparts except that the half-range minima have been shifted to slightly lower nadir angles because these mean extrema biases are more negative for given depths and nadir angles than those for the higher threshold, and the crossover point thus occurs at lower nadir angles. For a 20-m depth, the minimum is at 20° , and for a 15-cm bias uncertainty, the nadir angle range is 17° to 23° . The 30-m minimum is about 16 cm at 19.5° . In addition, a 20% LFT is not as desirable because the random error component is larger¹⁶. Because the range of unknown optical depths from 2 to 16 is quite large, it was felt that even marginally increased knowledge of that parameter might reduce the bias variations. To that end, the same procedure was repeated for the case where αD is known (or assumed) to be either less than or greater than 8. The resulting minimum half-range for $2 < \alpha D < 8$ is quite a bit smaller, but the half-range for $8 < \alpha D < 16$ is virtually the same as for $2 < \alpha D < 16$. This means that most of the total variation occurs at high αD s, and that much higher resolution in an αD estimate would be required to significantly reduce the bias variation.

Bias variation curves for HALS processing are qualitatively similar. For 6-ns difference and CFD delays and P_m/B varying between 1 and 10, the minimum half-range is 22 cm, and the curve is fairly flat from about 10° to 18° . The reason for the significant increase in the minimum bias variation is the added degree of freedom represented by P_m/B . Because the minimum value is unsatisfactorily large, specific information on P_m/B will be required. For cases with P_m/B fixed at values of 1 (Fig. 7) and 10, the half-range minima are 13–14 cm and occur at angles of 14° – 16° . A 15-cm level is not exceeded for nadir angle ranges of 12.5° – 19° and 9° – 18° for P_m/B s of 1 and 10, respectively. The net useful range with that constraint is thus 12.5° to 18° if P_m/B is measured for every return. The mean extrema biases for the given conditions are more negative than for LFTs, and they change more rapidly with varying nadir angle. As in the LFT case, performance for the high αD range is not significantly better than for the full range — the angular range below 15 cm is extended to 9° – 22° , but the minimum half-range is about the same. As seen in Fig. 8, increasing the difference delay from 6 ns to 15 ns increases the optimum nadir angle for an average P_m/B from 15° to nearly 20° as the bias functionalities become more similar to those for LFTs. The optimum nadir angle is slightly lower for a CFD delay of 3 ns and slightly higher for 10 ns. A 10-ns CFD delay is undesirable because the minimum is quite narrow, and also because detection generally occurs after the peak of the return waveform. The minimum bias variation for a 3-ns CFD delay is lower than for 6 ns, but the optimum angle of 12° tends to be a bit lower than desired in terms of coverage rate. If a 3-ns CFD delay is used, a longer difference delay, say 15 ns, would consequently be desirable to raise the optimum nadir angle.

Systems not operating within the optimal nadir angle range will experience uncertainties in depth measurement biases as functions of unknown water optical parameters which are significantly larger than international hydrographic accuracy standards permit. At nadir, for example, the bias variation for a 50% LFT algorithm is seen in Fig. 6 to be ± 37 cm at a 20-m depth and ± 47 cm at 30 m. These curves are flat, and bias variations remain large out to a nadir angle of 10° . For the HALS case in Fig. 7, the values are ± 26 cm and ± 31 cm, respectively. Even with limited ground truth measurements of optical properties, such errors are unavoidable due to the inherent patchiness of coastal waters.

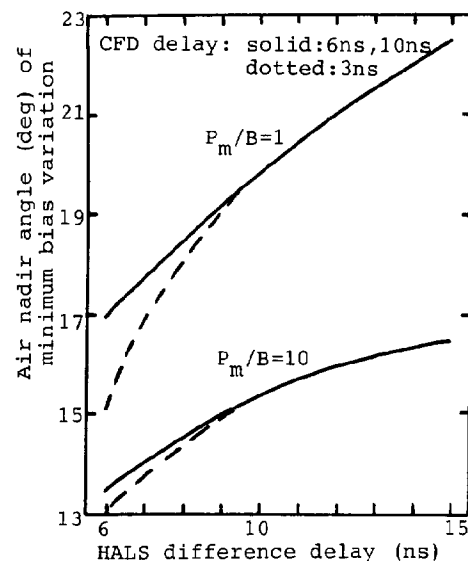
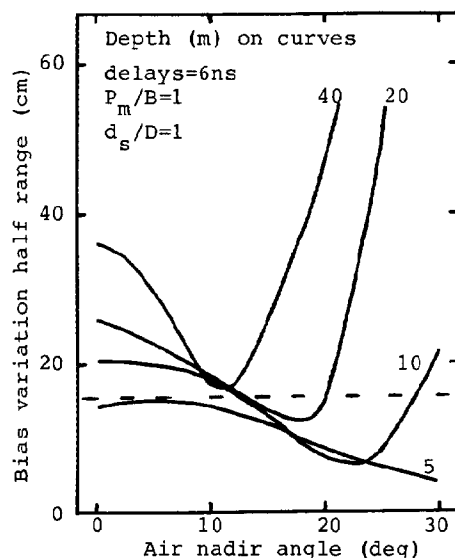


Figure 7. Bias variation half ranges for HALS(6ns,6ns, $P_m/B=1$). Figure 8. HALS optimum nadir angle versus difference delay.

Formal Bias Description

For use as bias correctors, the mean extrema biases can be either tabulated or fitted analytically. Smoothed biases tabulated at 5 m, 10 m, 20 m, 30 m, and 40 m can be interpolated linearly over depth and nadir angle, with very small residual errors, for nadir angles up to and including 25°. Alternately, if algebraic representations are desired, the biases can be described in the form

$$B(\text{cm}) = aD^n - bD^m(1 - \cos\theta)^k, \quad (3)$$

where B is the bias in centimeters, D is the depth in meters, and θ is the air nadir angle. The coefficients a, b, n, m, and k can be adjusted to fit the bias curves for various cases of signal processing algorithms and parameters. Table 2 presents sets of coefficients for the mean extrema bias curves along with their respective RMS of fit and maximum deviation of fit calculated for depths from 5 m - 20 m and nadir angles of 15°-25°. The fits themselves are valid from 0°-25° and for depths to 40 m, as well.

Case	a	b	n	m	k	RMS (cm)	max. dev. (cm)
LFT 50%	6.5	27.0	0.58	1.25	1.26	2.5	4.7
LFT 20%	8.3	21.5	0.46	1.16	0.98	1.3	2.3
HALS (6ns, 6ns), $P_m/B = 1$	17.8	13.0	0.26	1.60	1.19	1.6	5.0
HALS (6ns, 6ns), $P_m/B = 10$	10.3	20.0	0.32	1.40	1.08	2.4	4.9

Table 2. Bias Fitting Coefficients

Linear interpolation of tabulated values provides a slightly more accurate, if more cumbersome, representation of the simulation outputs, but it is possible that the inherent smoothing action of the analytic fit over all parameters may provide slightly more consistent results. Regardless of whether CFD biases are derived from tables or a formal expression, they will have to be calculated by interpolation or extrapolation from the two given values of $\log(P_m/B)$.

Conclusions

The impact of underwater light propagation mechanisms on the depth measurement accuracy of airborne laser hydrography has been investigated via a powerful new Monte Carlo computer simulation procedure. The simulation program provides a set of paths for downwelling photons arriving at the bottom for given sets of optical parameters and system variables. The resulting temporal and spatial distributions are used to compute impulse and actual source or "environmental" response functions at a distant, off-nadir, airborne receiver.

Scattering from particulate materials in the water column causes substantial spatial spreading of the beam. For typical operating optical depths, the half power beam width is about 28°. Detection of small targets is enhanced by leading edge pulse location algorithms. The resulting receiver field-of-view requirement for no significant reduction of peak return power is a full angle of 0.7D/H radians. For a 7-ns FWHM source pulse, the peak return power for a sufficient receiver FOV can be described as exponential with depth with a log slope of -2nK, where $1.1 < n(s, \theta) < 1.4$.

Depth measurement biases are calculated from environmental response functions, based on the 7-ns source pulse, for several typical signal processing and pulse location algorithms. These biases have been developed for bounding ranges of optical parameters in coastal waters and for all combinations of typical operational system variables. The only external input is the "phase function" scattering distribution. The sensitivity of the biases to phase function is small, but reported biases could differ somewhat from field data should the selected Petzold functions prove not to be representative.

Resultant biases may be either deep due to multiple scattering or shallow due to geometric undercutting, depending on nadir angle, water depth, and water optical properties. The strongest functionalities are with nadir angle and with signal processing and pulse location algorithms. It has been found that the net bias magnitudes can be large compared to international accuracy standards, and that the biases should therefore be corrected out of operational raw depth data.

These bias predictions could be used as bias correctors for operational data if all driving optical parameters — optical depth, phase function, and single-scattering albedo — were known. Because these parameters cannot be easily or accurately estimated from the air, however, a modified approach is required. It has been shown that for certain limited ranges of scanner nadir angles, whose magnitudes depend on signal processing protocol, the bias variations due to unknown water optical parameters are less than ±15 cm at a 20-m depth and ±20 cm at a 30-m depth. These optimal nadir angles, in the 15°-23° range, are appropriate for system operation in terms of desired swath width and aircraft altitude.

Constraining operations to preferred nadir angles via appropriate scanner design will permit "passive" bias correction using mean extrema biases which depend only on available information such as nadir angle, depth, and minor functionalities such as field of view and, for log/difference/CFD processing, signal-to-background ratio. For linear processing with a fractional threshold pulse location algorithm or for log/difference/CFD processing, the optimum nadir angle and mean extrema biases reported herein may be used for bias correction. For other signal processing and pulse location protocols, corresponding new mean extrema bias functionalities must be calculated, and new matching nadir angles must be selected for minimum bias variation.

Acknowledgment

The authors express gratitude to H. Sang Lee for his insightful criticism and to the Defense Mapping Agency, the Office of Naval Research, and the Naval Ocean Research and Development Activity who provided funding for a portion of this effort.

References

1. Thomas, R. W. L. and Guenther, G. C., "Theoretical Characterization of Bottom Returns for Bathymetric Lidar," Proceedings of the International Conference on Lasers '78, December 11 - 15, 1978, Orlando, Fla., Society for Optical and Quantum Electronics, McLean, Va., 48-59, 1979.
2. Plass, G. N. and Kattawar, G. W., J. Atmos. Sci., 28, 1187, 1971.
3. Petzold, T. J., "Volume Scattering Functions for Selected Ocean Waters," SIO Ref. 72-78, Scripps Institution of Oceanography, Visibility Laboratory, San Diego, Calif., 79 pp., 1972.
4. Gordon, H. R., "Mie Theory Models of Light Scattering by Ocean Particulates," Suspended Solids in Water, Plenum Press, Ed. Ronald J. Gibbs, 73-86, 1974.
5. Gordon, H. R., Brown, O. B., and Jacobs, M. M., "Computed Relationships Between the Inherent and Apparent Optical Properties of a Flat Homogeneous Ocean," Appl. Opt., 14, 417-427, 1975.
6. Timofeyeva, V. A. and Gorobets, F. L., "On the Relationship Between the Attenuation Coefficients of Collimated and Diffuse Light Fluxes," Izv., Atmospheric and Oceanic Physics (Acad. of Sci., USSR), 3, 291-296 (166-169 in translation), 1967.
7. Prieur, L. and Morel, A., "Etude Theorique du Regime Asymptotique," Cahiers Oceanographique, 23, 35, 1971.
8. Chandrasekhar, S., Radiative Transfer. Dover Publications, New York, N. Y., 385 pp., 1960.
9. Guenther, G. C. and Thomas, R. W. L., "Simulations of the Impact of Inhomogeneous Water Columns on the Temporal Stretching of Laser Bathymetry Pulses," NOAA Technical Report OTES 2, National Oceanic and Atmospheric Administration, Rockville, Md., 39 pp., 1981.
10. Duntley, S. Q., "Underwater Lighting by Submerged Lasers and Incandescent Sources," SIO Ref. 71-1, Scripps Institution of Oceanography, Visibility Laboratory, San Diego, Ca., 275 pp., 1971.
11. Lewis, C. A., Swamer, W. G., Prettyman, C., and Reinhardt, G. W., "An Optical Radar for Airborne Use Over Natural Waters," Proc. Symp. on The Use of Lasers for Hydrographic Studies, Sept. 12, 1973, NASA/Wallops Flight Center, Wallops Island, Va., U.S. National Aeronautics and Space Administration, Wallops Island, Va., 67-80, 1973.
12. Gordon, H. R., "Interpretation of Airborne Oceanic Lidar: Effects of Multiple Scattering," Appl. Opt., 21, 2996-3001, 1982.
13. Guenther, G. C., "Effects of Detection Algorithm on Accuracy Degradation from Logarithmic and Difference Processing for Airborne Laser Bathymetric Returns," NOAA Technical Report OTES 6, National Oceanic and Atmospheric Administration, Rockville, Md., 38 pp., 1982.
14. Moniteq Ltd., "Determination of Parameters of Significance for Accuracy Optimization of a Scanning Lidar Bathymeter," Final Report, Canadian Hydrographic Service Contract, Concord, Ontario, Canada, 129 pp., 1983.
15. Wilson, W. H., "Spreading of Light Beams in Ocean Water," Proc. SPIE Ocean Optics VI, October 23-25, 1979, Monterey, Calif., Society of Photo-optical Instrumentation Engineers, Bellingham, Wash., 208, 64-72, 1979.
16. Guenther, G. C. and Thomas, R. W. L., "Error Analysis of Pulse Location Estimates for Simulated Bathymetric Lidar Returns," NOAA Technical Report OTES 1, National Oceanic and Atmospheric Administration, Rockville, Md., 1981.